

Fenton-like Reactivity on Fe₃O₄ Nanozymes Driven by Charge Transfer and Interfacial Water

Verónica Muriel Sánchez, Enio Lima Jr., Juan Santiago Grassano, Pablo Germán Lustemberg, Marco Antonio Morales Ovalle, Marcelo Vasquez Mansilla, Juan Daneri, Darío Ariel Estrin, Elin Lilian Winkler,* and María Verónica Ganduglia-Pirovano*

Magnetite (Fe₃O₄) nanoparticles, widely recognized as inorganic nanozymes due to their enzyme-like catalytic activity, are emerging as effective heterogeneous catalysts for Fenton-like reactions, in which lattice iron activates hydrogen peroxide (H₂O₂) to generate reactive oxygen species. While hydroxyl radicals (•OH) are generally considered the primary reactive species, the underlying mechanism—particularly the possible involvement of a high-valent ferryl intermediate (Fe⁴⁺=O)—remains under debate. Here, surface-specific spectroscopy with density functional theory (DFT) calculations is used to elucidate the mechanism of H₂O₂ activation on Fe₃O₄ (001) surfaces. It is found that •OH production is driven by electron transfer from subsurface Fe²⁺ centers to adsorbed H₂O₂, accompanied by the transient formation of a ferryl species. Moreover, interfacial water plays an active role in modulating surface reactivity and stabilizing key reaction intermediates. These findings clarify the origin of radical formation in Fe₃O₄ nanozymes and offer mechanistic insight to guide the rational design of next-generation oxide-based catalysts for environmental and biomedical applications.

1. Introduction

Nanozymes—synthetic nanomaterials that replicate enzyme-like catalysis,—have rapidly evolved into a vibrant research field, bridging nanotechnology, chemistry, and biomedicine. Since their initial discovery, they have been reported to exhibit a remarkable diversity of activities, including peroxidase-, oxidase-, catalase-, and superoxide dismutase-like functions. Unlike natural enzymes, nanozymes are not restricted to biological scaffolds, but instead span a wide spectrum of material classes, ranging from metals and metal oxides to carbon-based nanomaterials and metal–organic frameworks. This structural and compositional diversity opens opportunities to tailor catalytic performance for applications in areas as varied as biosensing, environmental remediation, and therapeutic intervention.^[1]

V. M. Sánchez, J. S. Grassano, J. Daneri, D. A. Estrin
Instituto de Química Física de los Materiales, Medio Ambiente y Energía
INQUIMAE-CONICET-UBA
Intendente Güiraldes 2160, Ciudad Autónoma de Buenos Aires
C1428EGA, Argentina

V. M. Sánchez, J. S. Grassano, J. Daneri, D. A. Estrin
Universidad de Buenos Aires
Facultad de Ciencias Exactas y Naturales
Departamento de Química Inorgánica, Analítica y Química Física
Intendente Güiraldes 2160, Ciudad Autónoma de Buenos Aires
C1428EGA, Argentina

E. Lima Jr., M. A. Morales Ovalle, M. Vasquez Mansilla, E. L. Winkler
Departamento Magnetismo y Materiales Magnéticos
Gerencia de Física
Centro Atómico Bariloche
Av. Bustillo km 9,5 Río Negro, San Carlos de Bariloche R8402AGP,
Argentina
E-mail: elin.winkler@ib.edu.ar

E. Lima Jr., M. A. Morales Ovalle, M. Vasquez Mansilla, E. L. Winkler
Instituto de Nanociencia y Nanotecnología
Nodo Bariloche
CNEA-CONICET
Av. Bustillo km 9,5 Río Negro, San Carlos de Bariloche R8402AGP
Argentina

P. G. Lustemberg, M. V. Ganduglia-Pirovano
Instituto de Catálisis y Petroquímica
CSIC
Marie Curie 2, Madrid, Madrid 28049, Spain
E-mail: vgp@icp.csic.es

M. A. Morales Ovalle, E. L. Winkler
Instituto Balseiro
CNEA-UNCuyo
Av. Bustillo km 9,5 Río Negro, San Carlos de Bariloche R8402AGP
Argentina

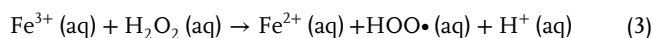
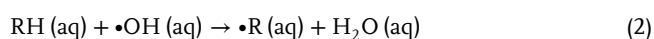
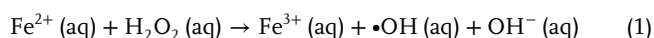
The ORCID identification number(s) for the author(s) of this article can be found under <https://doi.org/10.1002/sml.202507717>

© 2025 The Author(s). Small published by Wiley-VCH GmbH. This is an open access article under the terms of the [Creative Commons Attribution-NonCommercial-NoDerivs](#) License, which permits use and distribution in any medium, provided the original work is properly cited, the use is non-commercial and no modifications or adaptations are made.

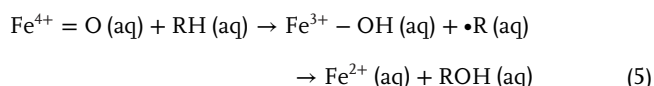
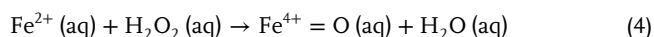
DOI: 10.1002/sml.202507717

Among metal oxide-based nanozymes, magnetite (Fe_3O_4) nanoparticles stand out due to their mixed-valence composition ($\text{Fe}^{2+}/\text{Fe}^{3+}$) and intrinsic magnetic properties, which facilitate efficient catalyst separation and reuse. These nanoparticles (NPs) exhibit strong peroxidase-like activity, catalyzing the decomposition of hydrogen peroxide (H_2O_2) under biologically and environmentally relevant conditions.^[2–9] Their catalytic behavior is primarily governed by $\text{Fe}^{2+}/\text{Fe}^{3+}$ redox cycling, supported by tunable surface chemistry, making them highly versatile for applications in environmental remediation, catalysis, and biomedicine.^[10–16] Furthermore, Fe_3O_4 NPs can be engineered to expose specific crystallographic facets, tailoring surface reactivity, while their high surface-to-volume ratio enhances catalytic efficiency.^[17] Such structural tunability and surface accessibility are particularly valuable for biomedical strategies that rely on localized reactive oxygen species (ROS) generation—such as antimicrobial treatments or oxidative stress-based cancer therapies including ferroptosis^[18,19]—as well as for environmental technologies involving pollutant degradation and advanced oxidation processes.^[20,21] Despite their broad utility, the mechanistic basis for H_2O_2 activation on magnetite surfaces remains incompletely understood. A long-standing debate concerns whether reactivity proceeds via classical radical chemistry—commonly referred to as the Haber–Weiss mechanism^[22]—or through the formation of a high-valent ferryl intermediate ($\text{Fe}^{4+}=\text{O}$), analogous to those observed in heme-containing enzymes.^[23] These two routes carry distinct implications for catalyst design, efficiency, and long-term stability, particularly given the redox-driven transformation of Fe_3O_4 into $\gamma\text{-Fe}_2\text{O}_3$, which diminishes activity over time.^[24] Understanding the atomistic origin of ROS production and transformations in Fe_3O_4 NPs is therefore essential for optimizing their performance across technological domains.

The Haber–Weiss framework (Equations 1–3), established following Fenton's pioneering discovery in 1894,^[25] describes hydroxyl radical formation through Fe^{2+} -mediated cleavage of H_2O_2 , subsequent substrate oxidation, and partial regeneration of Fe^{2+} via a slower Fe^{3+} reduction step.^[26–28]



While this radical-based chemistry has provided the foundation for understanding Fenton reactivity, an alternative view proposed by Bray and Gorin^[23] emphasizes the direct generation of ferryl species ($\text{Fe}^{4+}=\text{O}$), potent oxidants that can drive substrate oxidation without $\bullet\text{OH}$ free radical intermediates (Equations 4–5).



This ferryl-based mechanism is particularly intriguing because it parallels the catalytic cycles of peroxidases and cy-

tochromes P450, where high-valent iron–oxo intermediates act as the primary oxidants.^[29,30] Such analogies directly connect magnetite nanozymes to enzymatic systems, raising the question of whether their activity should be understood primarily through radical chemistry or through peroxidase-like ferryl pathways. Evidence for ferryl species has been reported both on hematite surfaces^[31,32] and, more recently, by Wan et al.^[33] on magnetite nanoparticles, where the PMSO probe method confirmed their transient formation during H_2O_2 activation. While such studies provide important precedent, direct spectroscopic detection of ferryl species remains challenging, and it is not yet clear under which conditions radical-based versus ferryl-based pathways dominate. This uncertainty highlights the need for combined experimental and theoretical approaches to clarify the mechanistic origin of reactivity in magnetite nanozymes.

A further challenge is the pH dependence of the homogeneous Fenton reaction, which requires acidic conditions ($\text{pH} < 4$) to suppress iron hydroxide precipitation. This has motivated interest in heterogeneous Fenton catalysis using solid-phase metal oxides, particularly Fe_3O_4 , which offer greater robustness.^[30] Magnetite adopts an inverse spinel structure, $[\text{Fe}^{3+}]_{\text{Td}}[\text{Fe}^{2+}\text{Fe}^{3+}]_{\text{Oh}}\text{O}_4$, with octahedral Fe^{2+} ions central to redox activity. Nanoparticles frequently expose the (001) facet. Among the low-index surfaces of Fe_3O_4 , the (001) and (111) facets are recognized as the most stable terminations, with the general trend in surface energies being $(100) < (111) < (110)$ across reasonable models.^[34] Importantly, the (001) facet undergoes a $(\sqrt{2} \times \sqrt{2})R45^\circ$ subsurface cation vacancy (SCV) reconstruction,^[35] in which all outermost cations are Fe^{3+} . This termination has been shown to be especially stable in the presence of water and under oxidizing conditions,^[36–38] making it a representative model surface for mechanistic studies of H_2O_2 activation. These structural features pose a central mechanistic question: can Fe_3O_4 (001) surfaces, which expose only Fe^{3+} at the top layer, still catalyze hydroxyl radical formation—or does their reactivity proceed via ferryl species more akin to enzymatic nanozymes?

Recent studies suggest that reactivity on Fe_3O_4 surfaces is not governed solely by surface composition. Dong et al.^[24] proposed a bulk-to-surface electron transfer mechanism in which subsurface Fe^{2+} donates electrons to surface-adsorbed H_2O_2 , with redox cycling sustained through atomic diffusion—a process coupled to gradual transformation into $\gamma\text{-Fe}_2\text{O}_3$. This transformation, however, diminishes the material's $\bullet\text{OH}$ -generating capacity,^[24,39] highlighting the need to understand charge transport mechanisms in nanoparticle systems.

Density functional theory (DFT) studies have provided valuable insights into H_2O_2 decomposition on Fe_3O_4 surfaces. Calculations on the (311) surface support the Haber–Weiss mechanism as energetically favorable,^[40] while others examining bulk-truncated (001) surfaces or Fe_3O_4 clusters have proposed either ferryl intermediates or adsorbed hydroxyl pathways.^[41–43] However, these models often omit solvent effects,^[40–43] despite the known influence of interfacial water on surface structure and reactivity.^[36,37,44–46] Water adsorption studies show that even with increasing hydration, only partial hydroxylation occurs, suggesting a nuanced role of solvent in stabilizing intermediates and modulating reactivity.

This leaves several key mechanistic questions unresolved: Does H_2O_2 cleavage proceed via homolytic or heterolytic bond scission? Does a ferryl intermediate form under catalytically relevant conditions? How does water modulate the energetics and surface states? Can these surface reactions explain the observed phase transition from Fe_3O_4 to $\gamma\text{-Fe}_2\text{O}_3$ during catalysis?

In this work, we address these questions through a combined experimental–theoretical approach. Using facet-specific synthesis of Fe_3O_4 nanoparticles that predominantly expose (001) surfaces, we employ electron paramagnetic resonance (EPR) to detect and quantify ROS, ferromagnetic resonance (FMR) to monitor structural evolution, and DFT calculations with explicit solvation to map atomistic reaction pathways. Our findings show that H_2O_2 decomposition is driven by electron transfer from subsurface Fe^{2+} centers to adsorbed H_2O_2 , forming hydroxyl radicals and promoting nanoparticle oxidation. We identify a metastable ferryl species ($\text{Fe}^{4+}=\text{O}$), whose formation parallels that in enzymatic systems, and demonstrate that interfacial water significantly alters the reactivity landscape by stabilizing key intermediates and modulating energy barriers. These insights clarify the surface and subsurface mechanisms underlying Fe_3O_4 -catalyzed ROS production and provide a foundation for rational design of nanozyme-based Fenton catalysts.

2. Results and Discussion

2.1. Synthesis and Characterization of the Nanoparticles

The Fe_3O_4 nanoparticles were synthesized by thermal decomposition of an organic salt precursor in the presence of benzyl ether and oleylamine as surfactants. TEM images reveal that the as-synthesized NPs exhibit uniform size distribution of 7.2 ± 0.5 nm and display polygonal morphology, with most particles presenting hexagonal 2D projections (Figure 1a,b). HRTEM images and the fast Fourier transform (FFT) analyses reveal crystalline planes that can be indexed to the (400), (220), and (111) reflections, with surface terminations mainly corresponding to the {111} and {100} facets (Figure 1b–e; Figure S1, Supporting Information). This is consistent with a truncated octahedral morphology, commonly observed under similar synthesis conditions.^[17,47–49] Variations in the degree of octahedral truncation lead to different relative proportions of {111} and {100} facets.^[47] Statistical analyses of 2D nanoparticle projections indicate that $\approx 54\%$ of the exposed surface corresponds to {100} facets. Because the experimentally predominant family is {100}, which includes the (001) plane, and surface-science studies have shown that Fe_3O_4 (001) reconstructs under oxidizing aqueous conditions into the $(\sqrt{2} \times \sqrt{2})\text{R}45^\circ$ subsurface cation vacancy (SCV) structure,^[35–38] we therefore adopt the reconstructed (001)-SCV termination as the representative surface model for the DFT mechanistic analysis.

X-ray powder diffraction (XRD) measurement confirms the Fe_3O_4 single-phase spinel structure with Fd-3m space group (Figure 1f). The Rietveld refinement yields a lattice parameter of $a = 8.3961(5)$ Å, which is in good agreement with the reported values for magnetite.^[48]

To assess the role of the iron ions' oxidation state in the reaction, a second system was prepared by oxidizing the as-

synthesized nanoparticles at 473 K in atmospheric air for 2 h. This treatment resulted in an increased Fe^{3+} content while preserving the spinel Fd-3m structure, thereby enabling a comparative study of the influence of iron valency on catalytic reactivity. The corresponding XRD pattern is shown in Figure 1f, and the Rietveld refinement yield a lattice parameter of $a = 8.350(1)$ Å, consistent with the reported values for $\gamma\text{-Fe}_2\text{O}_3$ (8.33–8.34 Å).^[49]

2.2. Reactivity and Free Radical Dynamics

The generation of free radicals during H_2O_2 decomposition on Fe_3O_4 NPs was monitored using spin-trapping EPR spectroscopy with 5,5-dimethyl-1-pyrroline N-oxide (DMPO) under acidic conditions.^[50,51] Hydroxyl and peroxy radicals were quantified based on their characteristic DMPO adducts, which extend their lifetime and produce distinct EPR signatures. However, these adducts undergo secondary oxidation over time. Notably, the DMPO- $\bullet\text{OH}$ adduct, the most abundant species, gradually decays over time, as the rate of $\bullet\text{OH}$ radical formation becomes slower than the rate of adduct degradation in the later stages of the reaction. The spectrum recorded 5 min after H_2O_2 addition (Figure 2a, top-left panel) reveals a convolution of EPR signals from various free radicals, along with the signal from the $\text{MgO}:\text{Mn}^{2+}$ internal standard used for intensity normalization. In the as-synthesized NPs, the $\bullet\text{OH}$ signal dominates the EPR spectrum, presenting the characteristic 1:2:2:1 quartet pattern associated with DMPO- $\bullet\text{OH}$ adducts. In contrast, $\bullet\text{OOH}$ and $\bullet\text{CH}_3$ radicals are barely detectable (Figure 2a, central panel). The $\bullet\text{OH}$ and $\bullet\text{OOH}$ radicals originate from H_2O_2 decomposition, while the $\bullet\text{CH}_3$ radical arises from secondary reactions of oxygen-based radicals with dimethyl sulfoxide (DMSO), which is used to dilute DMPO, as well as with residual organic material present on the nanoparticle surface. This interpretation is supported by EPR spectra of samples in which organic surface coatings were partially removed: under these conditions, the $\bullet\text{CH}_3$ signal becomes dominant (Figure S2, Supporting Information, central panels), confirming its association with residual organics and solvent interactions.

The $\bullet\text{OH}$ signal decays rapidly in Fe^{2+} -rich NPs, decreasing to $\approx 10\%$ of its initial intensity within 40 min (Figure 2a). Concurrently, ferromagnetic resonance (FMR) spectra of the same samples reveal a shift in the resonance field (H_R) from 3,450–3,267 G (Figure 2a, right panel), corresponding to a reduction in the anisotropy field (H_A) from 546–369 G. This shift is consistent with the complete oxidation of Fe_3O_4 to $\gamma\text{-Fe}_2\text{O}_3$, which is known to exhibit lower magnetic anisotropy.^[52]

The XRD pattern of the nanoparticles collected after the reaction (Figure 1f) further supports this conclusion, showing a peak shift toward higher angles relative to the as-synthesized sample, indicating a decrease in the lattice parameter. Rietveld refinement yields a lattice parameter of $a = 8.344(7)$ Å, consistent with a reduction in the unit cell volume in agreement with the value obtained for the thermally oxidized $\gamma\text{-Fe}_2\text{O}_3$ sample. Critically, these observations indicate that nanoparticle oxidation is driven by electron transfer from subsurface Fe^{2+} species to H_2O_2 , a process that facilitates hydroxyl radical generation and links bulk charge transport directly to surface reactivity.

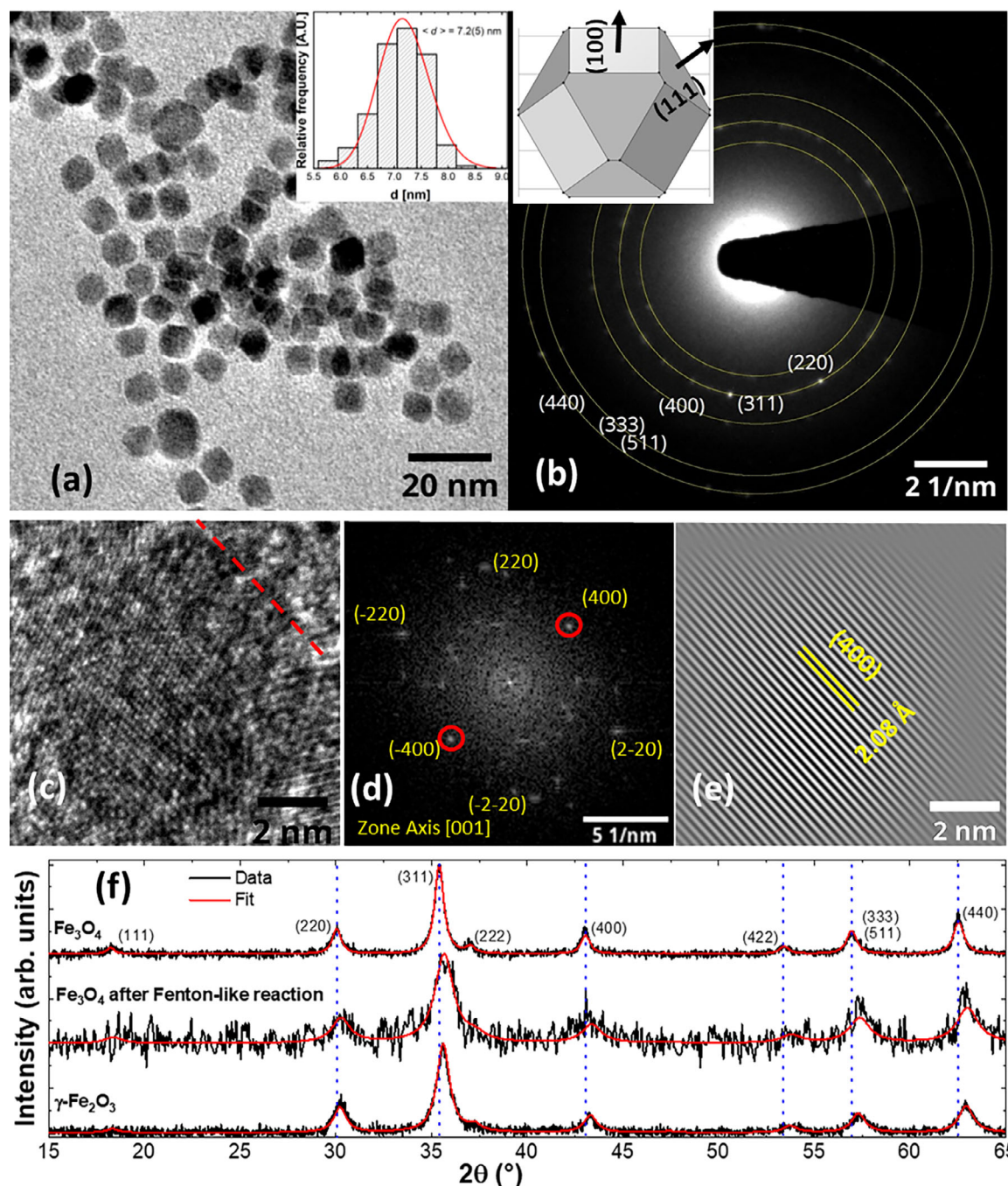


Figure 1. a) TEM image with size distribution histogram. b) Electron diffraction pattern indexed to the spinel structure with the nanoparticle geometrical model. c) HRTEM image showing hexagonal projection consistent with truncated octahedral morphology. d) FFT of panel (c), highlighting (004) and (220) planes. e) Inverse FFT reconstruction from the (400) diffraction spots. f) XRD pattern of the as-synthesized Fe₃O₄ nanoparticles and the oxidized samples after Fenton-like reaction and thermal treatment.

In contrast, oxidized Fe³⁺-rich nanoparticles show a roughly tenfold decrease in •OH production (Figure 2b). Under these conditions, •OOH and •CH₃ radicals persist at steady-state concentrations, consistent with the mechanisms described by Equations (3) and (1) (Figure 2b, central panel). It is worth noting that, although Fe₃O₄ to γ -Fe₂O₃ systems exhibit markedly different signals at the beginning of the reaction, at longer reaction times

the normalized EPR area of the free radicals tends to converge to similar values. This behavior is consistent with the interpretation that, over extended reaction times, the reactivity becomes dominated by Fe³⁺ species, which is slower and less efficient than the Fe²⁺-mediated process, in agreement with the classical homogeneous Fenton mechanism. Unlike Fe²⁺-rich NPs, the FMR spectra of Fe³⁺-rich nanoparticles remain unchanged following the

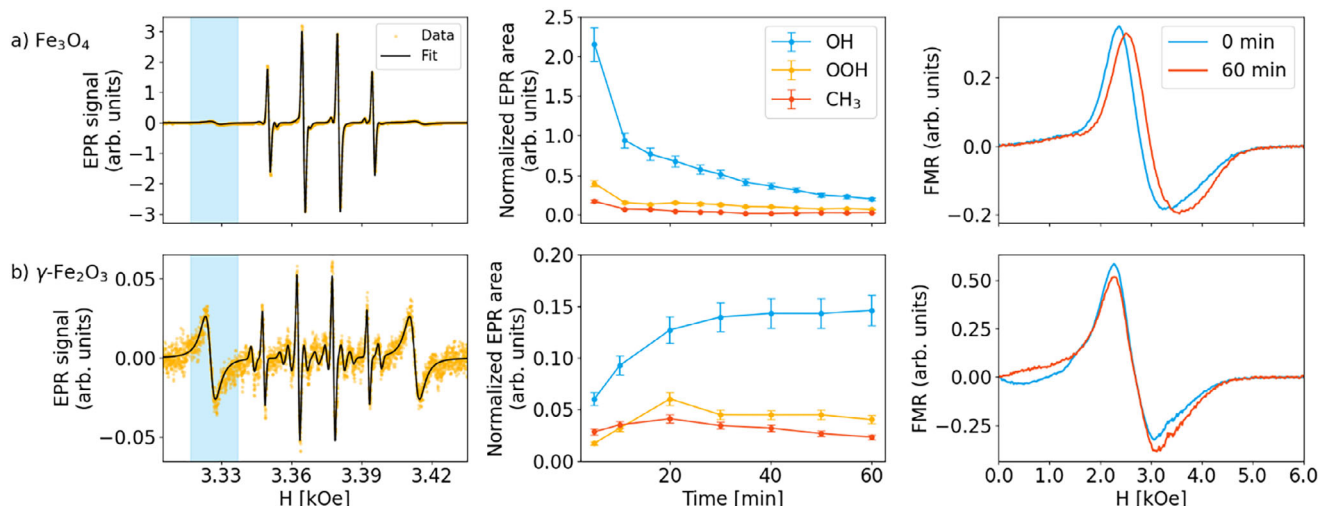


Figure 2. Radical generation and magnetic evolution during H_2O_2 decomposition on Fe_3O_4 nanoparticles. a) As-synthesized sample after organic layer removal. b) Oxidized sample. Left: EPR spectra 5 min after H_2O_2 addition. Center: Time evolution of $\bullet\text{OH}$, $\bullet\text{OOH}$, and $\bullet\text{CH}_3$ radical signals. Right: FMR spectra at 0 and 60 min.

reaction (Figure 2b, right panel), indicating negligible changes in the bulk sample—a characteristic feature of surface-limited reactivity.

These results highlight the pivotal role of Fe^{2+} in driving $\bullet\text{OH}$ radical generation during H_2O_2 decomposition, promoted by Fe_3O_4 nanoparticles, through a mechanism reminiscent of the homogeneous Fenton reaction. As Fe^{2+} is progressively oxidized, the $\bullet\text{OH}$ radical concentration diminishes until reaching a saturation point. Beyond this stage, the reaction is sustained by Fe^{3+} species, which exhibit markedly slower reactivity in both heterogeneous and homogeneous phases. Consequently, free radical production in Fe^{3+} -rich nanoparticles proceeds at a reduced rate, governed by the limited redox activity of Fe^{3+} -mediated pathways.

2.3. Molecular Mechanisms of Hydrogen Peroxide Decomposition

To elucidate the reaction mechanisms of hydrogen peroxide decomposition on Fe_3O_4 (001) surfaces, we performed systematic electronic structure calculations at the DFT level. The fully optimized models shown in Figure 3 each contain one adsorbed H_2O_2 molecule and correspond to three distinct surface conditions: a) a dry SCV (001) surface, b) a hydrated SCV (001) surface with a single water molecule positioned over the Fe_{Td} vacancy, forming a hydrogen bond with the O(2c) site, and c) a hydroxylated SCV (001) surface, modeled with three water molecules. In the latter case, one water molecule is molecularly adsorbed, a second dissociates to protonate an O(2c) site and hydroxylate an Fe_{Oh} site, and a third is placed above the Fe_{Td} vacancy. The placement of the water molecules was chosen to promote interaction with the H_2O_2 reactant and is consistent with previous studies.^[33,40] According to our calculations, the oxide surface retains the composition $(\text{Fe}^{2+}_{\text{Oh}})_5(\text{Fe}^{3+}_{\text{Oh}})_{21}(\text{Fe}^{3+}_{\text{Td}})_{13}\text{O}_{56}$ across all models. All surface-exposed iron atoms are in the Fe^{3+} state, while five Fe^{2+} ions occupy octahedral sites below the fourth atomic layer, contributing to a total magnetic moment of 60 μB per unit cell.

Structural parameters and Bader charge analyses are provided in Tables S1 and S2 (Supporting Information).

To gain insight into the H_2O_2 decomposition, we investigated two distinct bond cleavage routes: hydroxyl (HO-OH) and peroxy (H-OOH) dissociation. Figure 4a shows the reaction energy profiles, calculated using the climbing-image nudged elastic band (CI-NEB) method for the three Fe_3O_4 (001) surface models. Notably, for the hydroxyl pathway, we identified a well-defined state featuring a ferryl species ($\text{Fe}^{4+}=\text{O}$) and an adsorbed water molecule, which is slightly more stable than the configuration with two adsorbed hydroxyl radicals. This species, although likely short-lived, supports the mechanistic relevance of an alternative pathway (Equation 4), indicating that H_2O_2 decomposition proceeds via a ferryl intermediate—even when the final state consists of two hydroxyl groups, mirroring features observed in enzymatic systems. Figure 4b presents top views of the key reaction states, including reactants (R), transition states (TS1, TS2), intermediates (I), and products (P1, P2), for the model containing three water molecules. The proposed mechanisms are illustrated in Scheme 1 and will be discussed below, beginning with the case involving an adsorbed H_2O_2 molecule in the absence of water, to subsequently address solvent effects on reactivity.

2.4. Reactivity on the Dry Surface

2.4.1. Hydroxyl pathway (R-TS1-P1-I)

We propose that cleavage of the HO-OH bond results in the formation of two adsorbed hydroxyl groups, each positioned over a Fe_{Oh} atom (Figure S3 and Video S1, Supporting Information). The resulting product structure (P1) is more stable than the reactant state (R) by 0.66 eV, indicating an exothermic process (Figure 4a). The calculated activation barrier for this transformation is 0.80 eV. In the P1 configuration, the two hydroxyl groups form a hydrogen bond with each other, characterized by

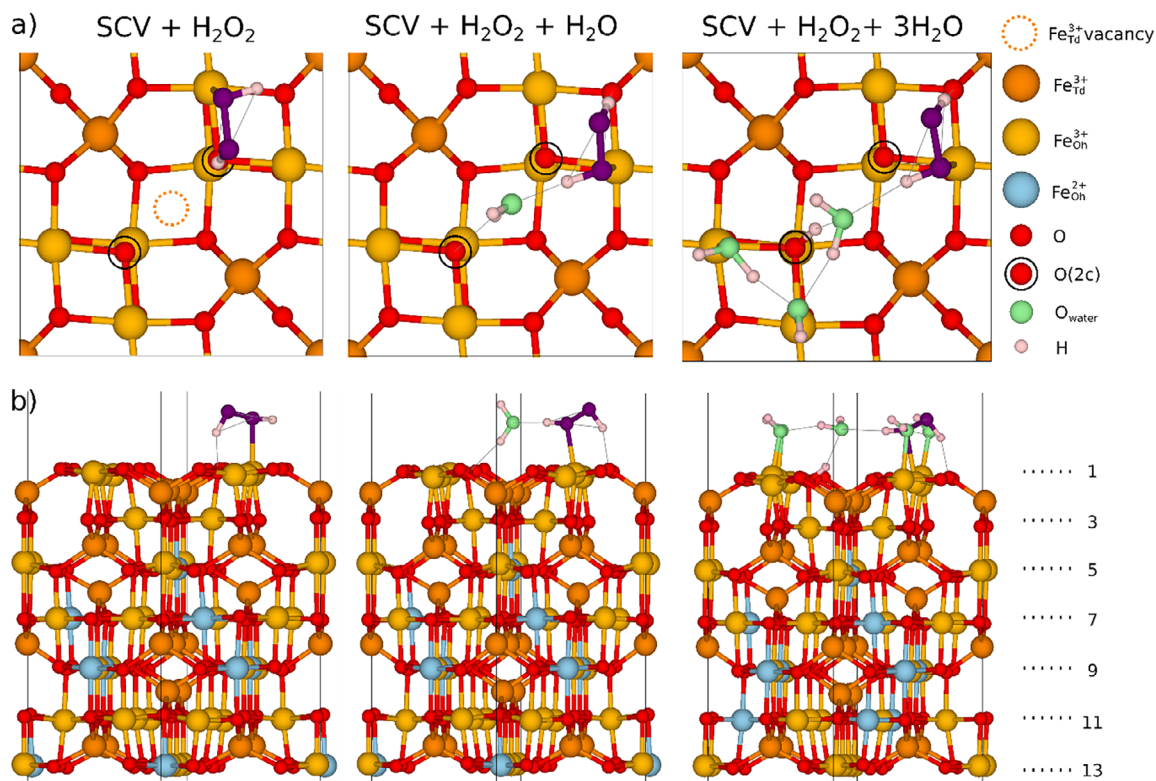


Figure 3. Figure 3. Optimized DFT models of Fe_3O_4 (001) surfaces with adsorbed H_2O_2 : dry, hydrated with one water, and hydroxylated with three waters. Top (a) and side (b) views are shown.

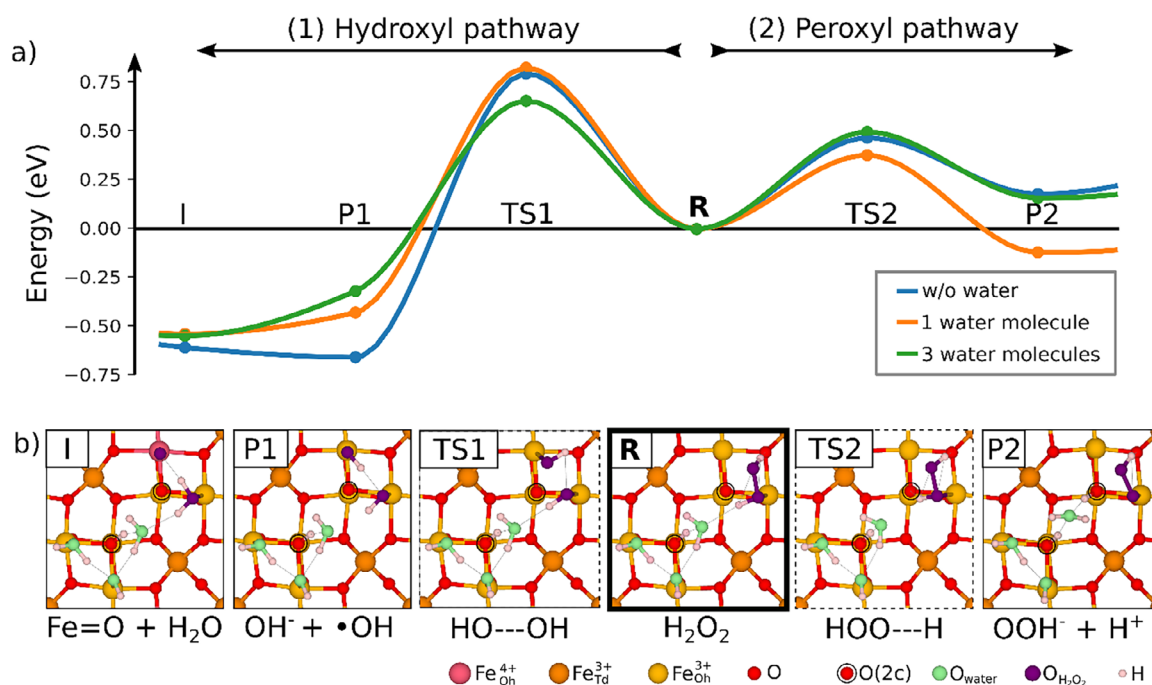
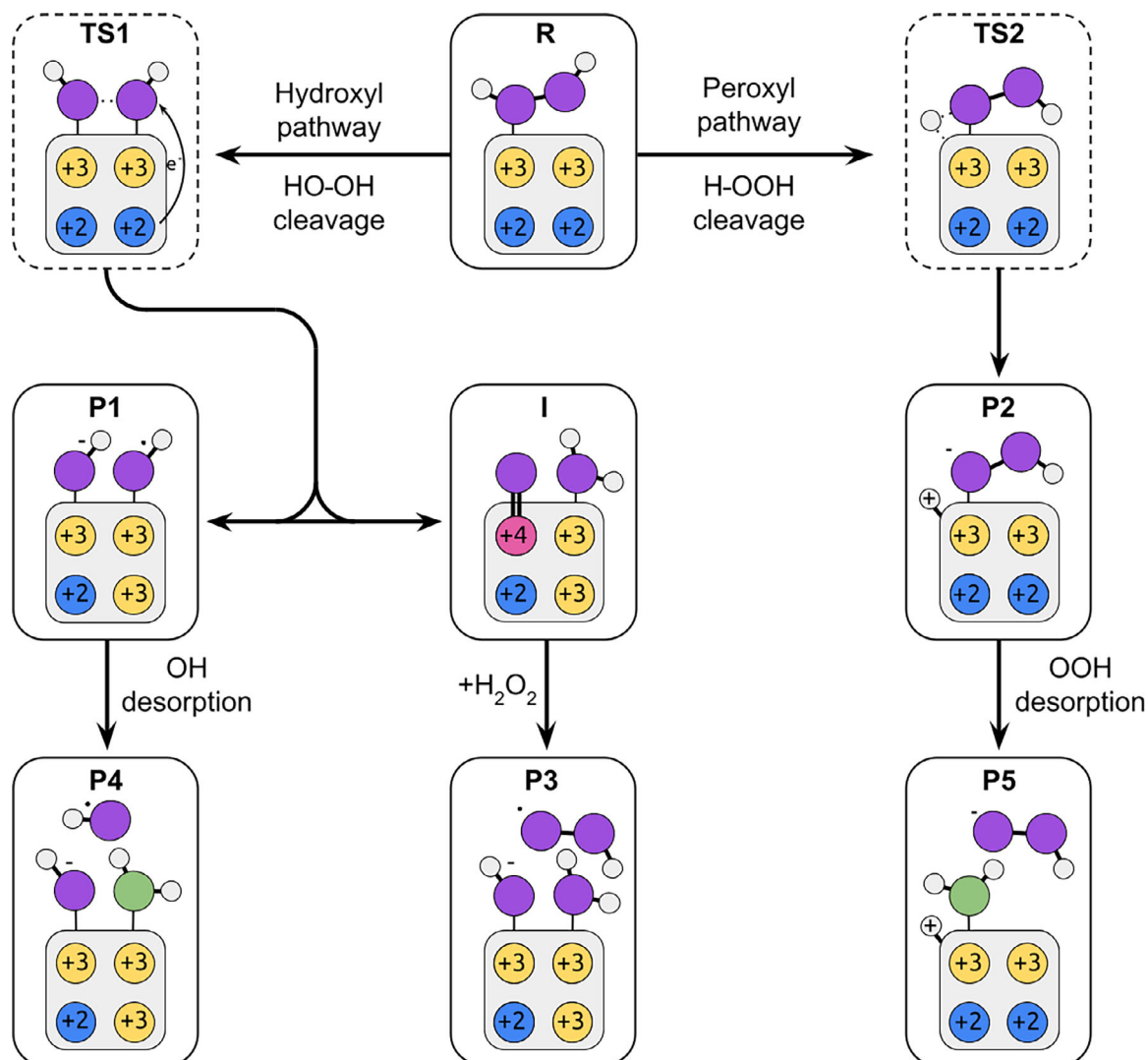


Figure 4. Reaction energy profiles and structures for H_2O_2 decomposition. a) Energy profiles for hydroxyl and peroxy pathways on dry and hydrated surfaces. b) DFT-optimized structures of key states (R, TS, I, P) with three water molecules; top views of the first three atomic layers are shown.



Scheme 1. Mechanistic pathways of H_2O_2 decomposition on hydroxylated Fe_3O_4 (001). Oxygen atoms from H_2O_2 in purple, from water in green. Iron atoms color-coded by oxidation state (Fe^{2+} blue, Fe^{3+} yellow, Fe^{4+} pink). Solid boxes: optimized structures; dashed boxes: transition states.

an $\text{H}_1\cdots\text{O}_2$ distance of 1.61 Å (Figure 5b; Figure S3, Supporting Information).

Analysis of the local magnetic moments of the Fe cations and atomic Bader charges along the reaction path (Figure 5c–e) reveals significant changes in P1 compared to R. The net Bader charge associated with the H_2O_2 fragment decreases from ≈ 0.0 to -0.86 |e|, indicating increased electron density localized on the oxygen atoms. Although the excess electron is distributed across both hydroxyl moieties, Bader charge analysis suggests it is more localized on the O_2 atom. As a result, the two hydroxyl groups can be described as a radical ($\bullet\text{O}_1\text{H}$) and an anion (O_2H^-), consistent with the classical Haber–Weiss mechanism (Figure 5e).

Strikingly, the P1 structure also exhibits a modified magnetic configuration compared to R (Figure 5c). Specifically, the magnetization of a $\text{Fe}^{2+}_{\text{Oh}}$ ion located in a deeper layer (Fe_{bulk}) in R shifts to a value consistent with that of a $\text{Fe}^{3+}_{\text{Oh}}$ ion ($\text{Fe}^{3+}_{\text{Oh}}$) in P1—

rising from $3.68 \mu_{\text{B}}$ in R to $4.16 \mu_{\text{B}}$ in P1. Consistently, the Bader charge of this cation (Fe_{bulk}) increases from 1.44 |e| in R to 1.80 |e| in P1 (Figure 5d). This change implies the occurrence of electron transfer from the subsurface $\text{Fe}^{2+}_{\text{Oh}}$ to the H_2O_2 moiety, taking place near the transition state (TS1). The resulting excess charge promotes $\text{O}_1\text{—O}_2$ bond cleavage and initiates the decomposition process. This interpretation is further supported by the density of states (DOS) of the TS1 structure (Figure S4, Supporting Information). Projected DOS analysis reveals that the dominant contributions near the Fermi level originate from the oxygen atoms of H_2O_2 and the Fe_{Oh} atom in the bulk that donates the electron, initially in a $\text{Fe}^{2+}_{\text{Oh}}$ state. The presence of partially filled states at the TS1 suggests transient charge delocalization between the adsorbate and the donor site. This electron transfer ultimately drives the progressive oxidation of the nanoparticles, in agreement with experimental observations of Fe_3O_4 transforming into $\gamma\text{—Fe}_2\text{O}_3$.

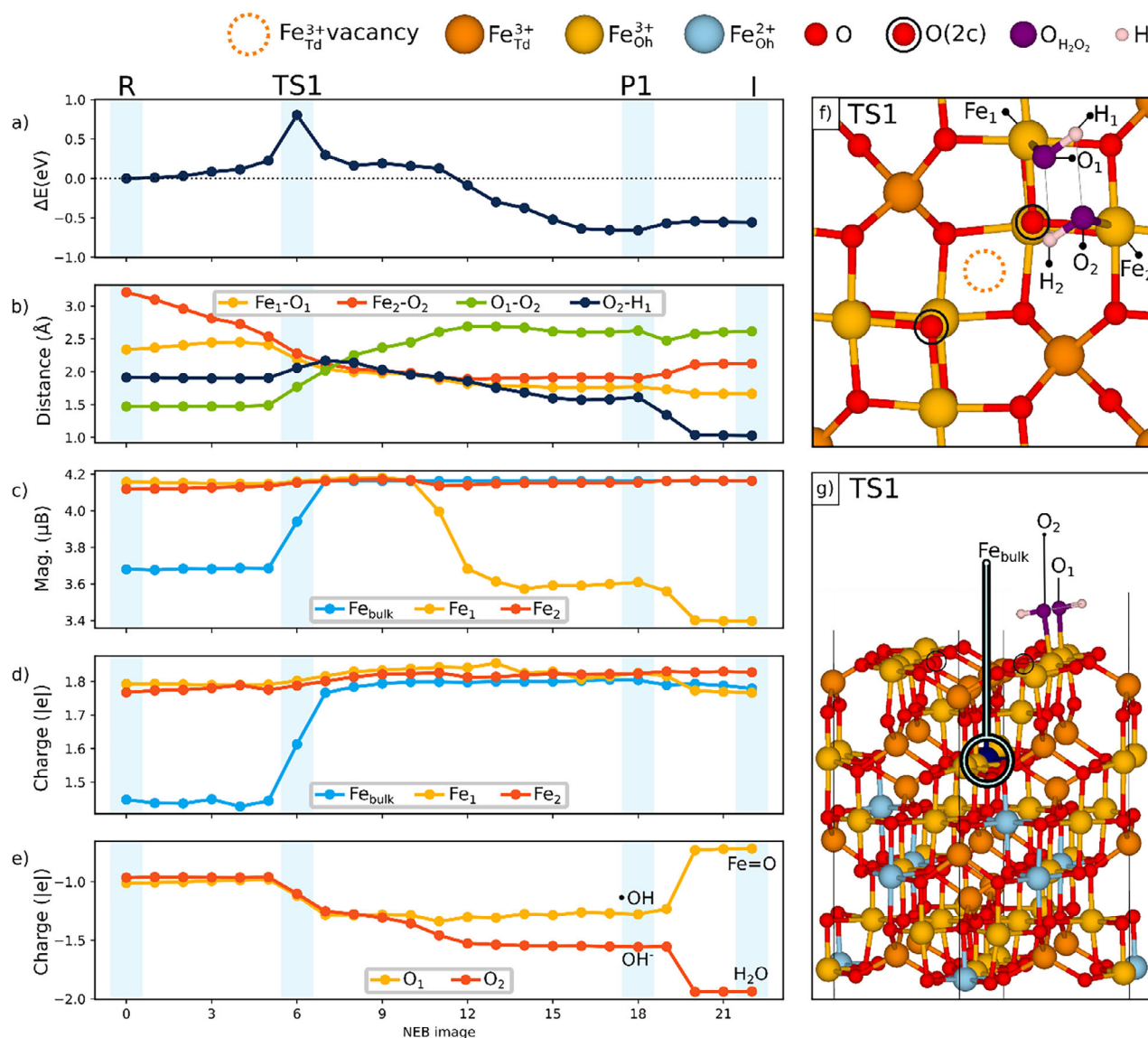
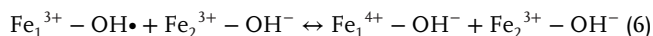


Figure 5. Hydroxyl pathway on the dry $\text{Fe}_3\text{O}_4(001)$ surface. NEB-calculated reaction path from R to P1 and I. Panels show: a) relative energies, b) bond lengths, c) magnetic moments, d,e) Bader charges, f) top view of TS1, and g) side view of the slab. The bulk Fe donating the electron is highlighted in dark blue.

A second significant change in magnetization is observed at a surface Fe_{Oh} site (Fe_1), in the structures following TS1 (Figure 5c). In the reactant state R, Fe_1 exhibits a magnetic moment of $4.16 \mu_{\text{B}}$ and a Bader charge of $1.79 |e|$, consistent with a $\text{Fe}^{3+}_{\text{Oh}}$ ion. In the P1 state, its magnetic moment decreases to $3.61 \mu_{\text{B}}$, corresponding to a configuration with four unpaired spin-up electrons—formally compatible with either Fe^{2+} or a Fe^{4+} oxidation state. However, the Bader charge remains essentially unchanged, indicating that Fe_1 is not reduced to Fe^{2+} and is instead more consistent with a formal Fe^{4+} state. In contrast, Fe_2 shows no significant change in either magnetic moment or Bader charge, consistent with the formation of a $\text{Fe}_2^{3+}\text{-O}_2\text{H}^-$. The $\text{Fe}_1\text{-O}_1$ bond length is 1.77 \AA , significantly shorter than the $\text{Fe}_2\text{-O}_2$ bond, which measures 1.91 \AA . This supports the interpretation that Fe_1 ultimately forms a ferryl species ($\text{Fe}^{4+}=\text{O}$), which is typ-

ically associated with shorter $\text{Fe}=\text{O}$ bonds than those found in $\text{Fe}^{3+}\text{-O}$ or $\text{Fe}^{2+}\text{-O}$ configurations. This interpretation is consistent with the ferryl intermediate reported for the $\{111\}$ surface of magnetite by Wan et al.^[33] Motivated by this precedent, we performed in situ IR spectroscopy to search for the characteristic $\text{Fe}^{4+}=\text{O}$ stretching vibration predicted by our DFT calculations at $\approx 765 \text{ cm}^{-1}$. However, this region is dominated by broad Fe-O absorption bands^[53] (Figure S5, Supporting Information), which mask any weaker ferryl signal. The inability to directly detect this mode is consistent with the transient nature and low surface concentration of ferryl intermediates. Taken together, the computational evidence presented here and the available experimental precedents strongly support the plausibility of ferryl species in Fe_3O_4 -catalyzed H_2O_2 decomposition, while underscoring the inherent challenges of their direct spectroscopic observation.

To rationalize the electronic reconfiguration at the Fe₁ site, the system can be represented by the following resonance structures, assuming formal oxidation states:



We note that this Fe₁⁴⁺–OH[–] + Fe₂³⁺–OH[–] state is distinct from the well-defined state **I** (Figure S3, Supporting Information), which corresponds to Fe₁⁴⁺=O + Fe₂³⁺–H₂O and features a *true* Fe₁⁴⁺=O ferryl species at Fe₁, with a water molecule adsorbed at the Fe₂ site. This observation prompted a closer investigation of the interconversion between hydroxyl and ferryl configurations. We found that state **I** is energetically close to **P1**, with an energy difference of only 0.05 eV. A NEB calculation between the two states revealed no energy barrier, and no transition state could be located, indicating that the system can transition between the two configurations in a barrierless manner. Given the high reactivity typically associated with ferryl (Fe⁴⁺=O) species, this state is likely to be highly reactive and therefore short-lived—further supporting its role as a transient intermediate along the reaction pathway.

Structurally, the key differences between **P1** and **I** lie in the position of the shared hydrogen atom and in the Fe–O bond lengths. In **P1**, the system adopts a Fe₁³⁺–OH...OH–Fe₂³⁺ hydrogen bonding arrangement, whereas in **I**, it forms a Fe₁⁴⁺=O...H–OH–Fe₂³⁺ configuration. The already short Fe₁–O bond length of 1.77 Å in **P1** further contracts to 1.66 Å in **I** (Figure 5b). Notably, the magnetic moment of Fe₁ decreases from 3.61 μ_B in **P1** to 3.40 μ_B in **I**, while the Bader charge remains essentially unchanged—consistent with the formation of a ferryl (Fe⁴⁺=O) species at the Fe₁ site. These spin and charge evolutions highlight the sequential transformation of surface Fe_{OH} sites and support the coexistence of multiple redox species—Fe³⁺–OH[–], Fe³⁺–•OH, and Fe⁴⁺=O—along the reaction pathway. The transformation between these states involves a hydrogen transfer between oxygen atoms, accompanied by an electronic rearrangement at the Fe site.

2.4.2. Peroxyl Pathway (**R** – **TS2** – **P2**)

For the cleavage of the H–OOH bond, we propose that a hydrogen atom is transferred from H₂O₂ to the closest O(2c) atom, resulting in an adsorbed peroxyl species (Fe³⁺_{OH}–OOH) and a protonated O(2c) (Figure S6 and Video S2, Supporting Information). The reaction has an activation barrier of 0.47 eV and is slightly endothermic, with a reaction energy of +0.18 eV (Figure 4).

The net Bader charge for the peroxyl (OOH) moiety in the final state **P2** indicates a partial anionic character, with a value of –0.54 |e|. In contrast to the hydroxyl cleavage pathway, this process does not trigger any significant rearrangement in the magnetization of surface Fe cations (Figure S7, Supporting Information). Instead, two concerted redox transitions occur between Fe_{OH} atoms in the bulk: one Fe atom in the 13th layer is oxidized from Fe²⁺ to Fe³⁺, concurrently with the reduction of a Fe³⁺ atom in the 11th layer, while a second electron exchange occurs between Fe_{OH} atoms in the 5th and 7th layers. As a result, this mechanism does not produce a net reduction of surface Fe sites, differing fundamentally from the pathway proposed for the homogeneous Fenton reaction (Equation 3). These findings suggest that regeneration of

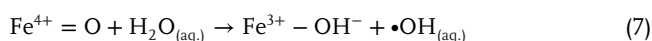
Fe²⁺ via direct H₂O₂ decomposition is unlikely to occur on this surface.

2.5. Solvent Effects on Reactivity

As the experimental reaction occurs at the solid-liquid interface, the inclusion of solvent water molecules is necessary to accurately represent the system. To this end, we investigated the role of water in the reaction mechanism by performing simulations of hydrated surface models, incorporating one and three water molecules into the system (Figure 3; Figures S8, S9, S10, and S11 and Videos S3, S4, S5, and S6, Supporting Information). For the hydroxyl pathway, the energy barrier is 0.86 eV with one water molecule (Figure 4a), which is comparable to the barrier on the dry surface (0.80 eV) and decreases to 0.66 eV in the model containing three water molecules. This reduction can be attributed to stabilization of the **TS1** structure by hydrogen bonding networks (Figure 4b). In both hydrated models, the reaction becomes less exothermic than that of the dry surface, with reaction energies of –0.40 and –0.34 eV for the systems with one and three water molecules, respectively, compared to –0.66 eV in the absence of water. As in the dry surface case (O₂–H₁, Figure 5b), the **P1** structure features a hydrogen bond between the adsorbed hydroxyl groups, with O...H distances of 1.50 and 1.69 Å for the systems with one and three water molecules, respectively (Figures S12 and S13, Supporting Information). In both cases, the hydroxyl group acting as the hydrogen bond acceptor is the more negatively charged species.

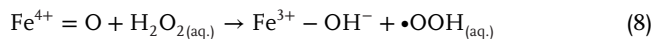
Similar trends to those observed on the dry surface are found in the magnetization of the cations and in the atomic Bader charges for the hydrated systems. A bulk Fe²⁺ ion donates an electron, and the H₂O₂ moiety becomes negatively charged. In the **P1** structures, the Fe₁ site exhibits a magnetization compatible with a Fe⁴⁺ oxidation state, while the associated hydroxyl group is slightly more negatively charged than a typical free radical. This behavior can be described by resonance structures of the form Fe₁³⁺–O₁H• ↔ Fe₁⁴⁺–O₁H[–], as discussed above. For the systems containing water, no significant energy barrier is found for the interconversion between the **P1** and ferryl **I** configurations. Notably, in the model with one water molecule, the **I** state emerged naturally as a stable intermediate along the NEB path between **R** and **P1** (Figure S12, Supporting Information). However, in contrast to the dry surface, where the energy difference is –0.05 eV, the **I** state becomes more stable than **P1** by –0.14 and –0.19 eV for the systems with one and three water molecules, respectively (Figure 4a).

As noted above, the Fe⁴⁺=O ferryl state is likely to be transient due to its high reactivity, supporting its role as an intermediate. The transition from state **I** to **P1** involves a proton transfer from the water adsorbed at the Fe₂ site; however, this is not the only possible reaction pathway for the ferryl species. For instance, water from the second hydration layer may react with the ferryl oxygen, generating a hydroxyl radical directly in solution without requiring desorption from the surface, according to:



Another possibility for the ferryl species is its reaction with an additional H₂O₂ molecule (Figure S14, Supporting Information),

yielding a hydroxyl group adsorbed on $\text{Fe}_1^{3+}\text{OH}$ and a peroxy radical released into the solvent:



We performed a NEB calculation for this process using the model containing three water molecules. The reaction is strongly exothermic, with a reaction energy of -0.84 eV, and exhibits a very small energy barrier—likely a consequence of the high reactivity of the ferryl species (Figure S15, Supporting Information). In the reactant state, the Fe_1 atom (associated with the $\text{Fe}^{4+}=\text{O}$ moiety) has a magnetic moment of $3.38 \mu_B$ and a Bader charge of $1.75 |e|$. Upon completion of the reaction, its magnetic moment increases to $4.17 \mu_B$, and the Bader charge rises to $1.83 |e|$, indicating reduction to a Fe^{3+} oxidation state. This redox change occurs concertedly with the hydrogen transfer from H_2O_2 to the ferryl oxygen, forming an OOH moiety with a net Bader charge of $-0.07 |e|$, consistent with its radical character. While the formation of peroxy species via this pathway depends on the transient availability of the ferryl intermediate, it may become significant under conditions of elevated H_2O_2 concentrations. This could account for the small amounts of peroxy radicals observed experimentally.

For the peroxy pathway in the model with one water molecule, we propose that the proton from H_2O_2 is transferred to the water molecule, accompanied by a concerted transfer of a proton from water to an O(2c) atom in a Grotthuss-like mechanism (Figure S10, Supporting Information). In this configuration, the most stable final state corresponds to the proton being transferred to the O(2c) atom furthest from the $\text{Fe}_{\text{OH}}-\text{OOH}$ group. This process has an energy barrier of 0.38 eV and a reaction energy of -0.12 eV (Figure 4a; Figure S16, Supporting Information). The corresponding transition state (TS2) exhibits an imaginary frequency associated with the concerted proton transfers (Table S3, Supporting Information), confirming the proposed mechanism.

In the model with three water molecules, one of the O(2c) atoms is already protonated due to the prior dissociation of a water molecule (Figures 4; Figure S9, Supporting Information). As a result, the hydrogen from H_2O_2 has only one available adsorption site. Similar to the dry surface case, we propose that the proton is transferred directly to the nearest O(2c) atom, yielding comparable values for the energy barrier and reaction energy (Figures 4a; Figure S17, Supporting Information). In both hydrated models, no substantial changes in the magnetization of the surface cations were observed (Figures S16 and S17, Supporting Information).

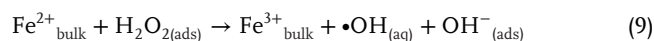
To evaluate the impact of bulk solvation, we combined the explicit three-water configurations with the implicit solvent model in VASPsol++.^[54] The results (Table S3, Supporting Information) show that while implicit solvation preferentially stabilizes charge-separated states such as the ferryl intermediate, the overall mechanistic trends remain unchanged compared to explicit water alone. This indicates that our qualitative conclusions are robust with respect to solvation treatment.

2.6. Desorption of Solvated Products

An accurate description of the solvent environment is essential for analyzing product desorption. To address this issue, we performed structural optimizations for both adsorbed and desorbed

configurations of the hydroxylated surface, including up to 12 explicit water molecules (Figures 6, 7, and Scheme 1). In the desorbed state, the original adsorbed product was replaced by a molecularly adsorbed water molecule on the corresponding Fe_{OH} site, while the desorbed product itself was surrounded by solvating water molecules. For comparison, we also computed desorption energies for the dry surface model (i.e., without water molecules).

For the hydroxyl pathway products (P1), we evaluated the desorption energy of each hydroxyl group while keeping the other adsorbed on the surface. The hydroxyl bound to Fe_1 —the hydrogen donor—exhibits a desorption energy of 0.22 eV (Figure 6). The desorbed OH species retains radical character, with a net Bader charge of $\approx -0.1 |e|$ and a projected magnetic moment of $-0.53 \mu_B$ on the oxygen atom. The second hydroxyl, acting as the hydrogen bond acceptor, shows a slightly lower desorption energy of 0.15 eV (Scheme 1). This species also displays radical character in solution, with a net Bader charge of $-0.3 |e|$ and an oxygen magnetic moment of $-0.47 \mu_B$. In both cases, the surface loses one electron, resulting in a total of four Fe^{2+} ions in the slab. The overall transformation from R to P4 (Scheme 1) follows the same stoichiometry as the Haber-Weiss reaction (Equation 1):



with the distinction that the OH^- remains coordinated to an iron cation in the heterogeneous context.

Desorption of the peroxy species involves a higher energy cost of 0.46 eV (P2 \rightarrow P5, Scheme 1 and Figure 7). The solvated OOH moiety exhibits anionic character, while the Fe_3O_4 surface retains five Fe^{2+} ions in the bulk. Given the high pKa value of H_2O_2 , this anion is expected to be protonated and converted into H_2O_2 in acidic aqueous conditions. The relatively high desorption energy suggests that the $\text{Fe}^{3+}\text{OH}-\text{OOH}$ configuration may exhibit significant stability. This could allow it to receive a proton from solution, potentially promoting O—OH bond cleavage and leading to the formation of a ferryl intermediate and a water molecule—analogue to the mechanism proposed in heme peroxidases (P2 \rightarrow I, Scheme 1). However, this step was not explicitly investigated in the present study.

Notably, the solvent environment has a profound effect on product desorption. In the absence of water molecules, the calculated desorption energies are substantially higher: 2.44 and 3.14 eV for the two hydroxyl species, and 2.04 eV for the peroxy.

3. Conclusion

By combining atomistic simulations with complementary experiments, we establish a mechanistic framework for hydrogen peroxide decomposition on magnetite (Fe_3O_4) nanoparticles. Our results show that the hydroxyl radical pathway predominates, supported by agreement between EPR kinetics and DFT+U energetics. Simulations further suggest a transient involvement of high-valent ferryl ($\text{Fe}^{4+}=\text{O}$) species, potentially expanding the reaction landscape beyond the classical radical mechanism.

Reactive species generation originates from electron transfer between bulk Fe^{2+} and adsorbed H_2O_2 , with explicit water molecules modulating key proton transfer steps and stabilizing intermediates. However, progressive Fe^{2+} oxidation leads

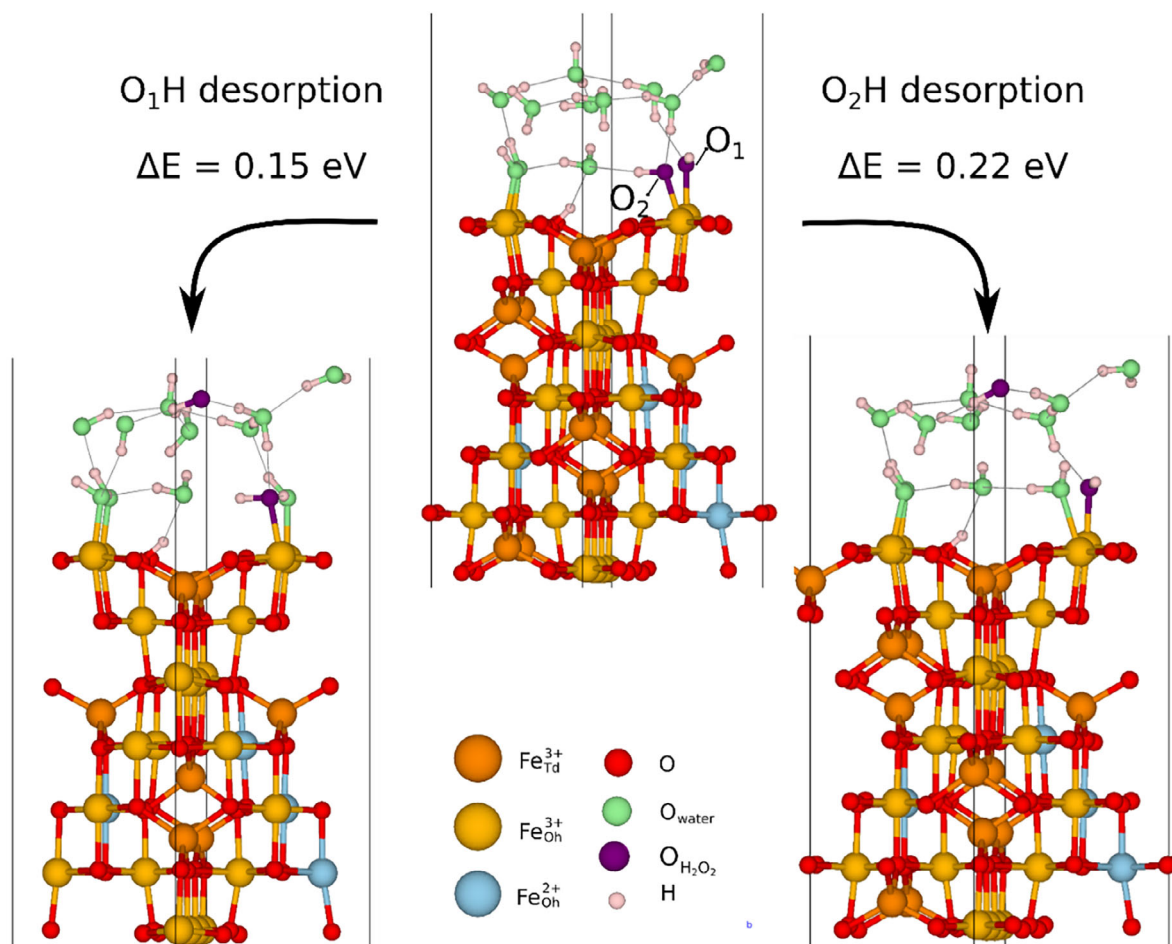


Figure 6. Adsorption and desorption of hydroxyl species on $Fe_3O_4(001)$. Side views of optimized structures: fully adsorbed state (center), desorbed O_1H (left), and desorbed O_2H (right).

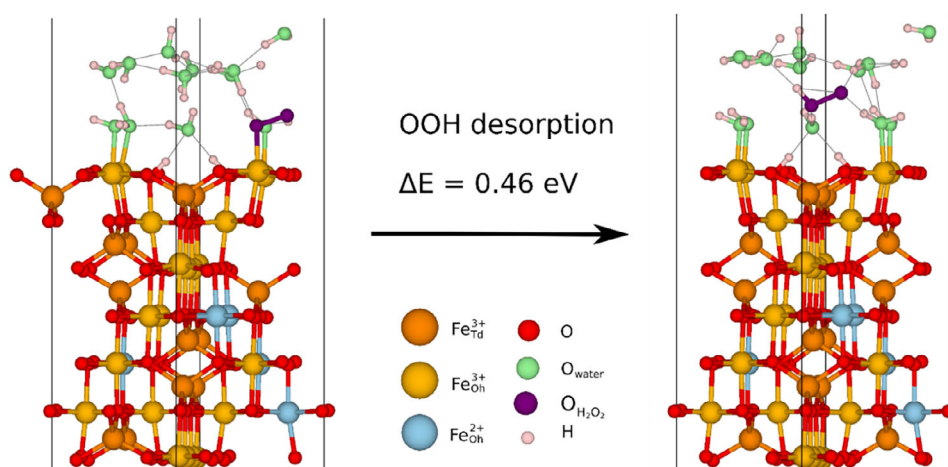


Figure 7. Adsorption and desorption of peroxy species on $Fe_3O_4(001)$. Left: adsorbed OOH configuration. Right: desorbed OOH into the solvated environment.

to catalyst deactivation, consistent with the observed transformation of Fe_3O_4 into less active $\gamma\text{-Fe}_2\text{O}_3$. These findings deepen our molecular understanding of how structure, surface chemistry, and redox state govern reactivity in iron oxide nanozymes. They also point to strategies for improving long-term performance—such as Fe^{2+} stabilization through electron-donating additives, surface functionalization, or photochemical redox regeneration—supporting the development of more robust and tunable Fenton-like catalysts for environmental and biomedical applications.

4. Experimental Section

Synthesis of the Nanoparticles—Chemicals: The reagents used for nanoparticle synthesis included iron (III) acetylacetonate ($\text{Fe}(\text{acac})_3$, 97%), oleic acid ($\geq 98.5\%$, analytical standard), and benzyl ether (98%), all purchased from Sigma-Aldrich or Supelco. To remove the organic coating formed during synthesis, the nanoparticles were washed sequentially with methanol ($\geq 99.5\%$), acetone ($\geq 99.5\%$), and toluene (99.8%), also obtained from Sigma-Aldrich. High-purity nitrogen gas (N_2 , 5.0 grade) was supplied by White-Martins and used as an inert atmosphere during synthesis.

Synthesis Protocol: Iron oxide nanoparticles were synthesized by thermal decomposition of an organometallic precursor in benzyl ether. In a 3-neck round-bottom flask equipped with a mechanical stirrer, 2 mmol of $\text{Fe}(\text{acac})_3$, 5 mmol of oleic acid, and 15 mL of benzyl ether were combined and stirred under a continuous nitrogen flow ($\approx 3.7 \text{ L min}^{-1}$). The mixture was gradually heated from room temperature to 300°C at a rate of $\approx 7^\circ\text{C min}^{-1}$. Once at reflux, the reaction was maintained for 5 h. After completion, heating was stopped, the nitrogen flow was turned off, and the system was allowed to cool naturally to room temperature. The resulting product was a dense, dark, homogeneous, and magnetically responsive colloidal solution.

Due to residual oleic acid capping formed during synthesis, the as-prepared nanoparticles exhibited hydrophobic behavior. To enable aqueous dispersion, the organic layer was removed using a two-step purification process. First, the nanoparticles were dispersed in methanol for 8 h, followed by chemical etching in acetone at 40°C for 48 h. The successful removal of organic residues was confirmed by Fourier transform infrared (FTIR) spectroscopy.

NPs Structural Characterization: The morphology and size distribution of the nanoparticles were analyzed using transmission electron microscopy (TEM). Micrographs were acquired with a FEI Tecnai T20 and Tecnai F30 microscopes, operated at 200 and 300 kV, respectively, at room temperature. TEM samples were prepared by depositing a drop of a dilute nanoparticle suspension onto an ultra-thin carbon film supported on a copper grid, followed by solvent evaporation under ambient conditions.

Particle size analysis was performed using ImageJ 1.54f software. The diameter of each nanoparticle was estimated by fitting a circle to its outline, and the resulting size distribution was fitted to a log-normal function to extract the mean diameter and standard deviation.

Structural characterization was carried out by X-ray diffraction (XRD) using a Bruker D8 Advance powder diffractometer equipped with a $\text{Cu K}\alpha$ radiation source ($\lambda = 0.1540593 \text{ nm}$), operating at room temperature. For sample preparation, a concentrated suspension of washed nanoparticles in toluene was drop-cast onto a rounded glass substrate and allowed to dry completely prior to measurement.

Electron Magnetic Resonance Spectroscopy Measurements: Electron paramagnetic resonance (EPR) and ferromagnetic resonance (FMR) spectra were recorded using a Bruker ELEXSYS II-E500 spectrometer equipped with an X-band resonant cavity (9.4 GHz), operating at 305 K. EPR spectra were acquired with a 10 dB attenuation (corresponding to 20 mW microwave power) and a modulation field amplitude of 1 Oe.

Based on the reported pH dependence of Fe_3O_4 reactivity, optimal between pH 3.5–5.5;^[55] and the onset of nanoparticle leaching below pH

5,^[56] the EPR experiments were performed at pH 5 to ensure efficient radical generation while minimizing Fe_3O_4 dissolution. For this, nanoparticle suspensions were prepared by dispersing 100 μg of Fe_3O_4 nanoparticles in 200 μL of a 10 mM acetate buffer solution (pH 5). To this, 50 μL of a 30% w/v solution of DMPO in DMSO was added as a spin-trapping agent, followed by the addition of 5 μL of 30% H_2O_2 to initiate the reaction. Spectra were recorded in quartz capillary tubes (Q-band, 1 mm internal diameter), with each measurement including an MgO crystal doped with a known concentration of Mn^{2+} , which served as an internal reference standard for signal quantification.

Spectral analysis was performed using SPIN software (Bruker), following a standardized fitting procedure. A third-order polynomial baseline correction was applied to remove the ferromagnetic background signal from the nanoparticles and resonator cavity. Paramagnetic resonance signals were then fitted using the hyperfine parameters corresponding to five radical species: DMPO adducts of $\bullet\text{OH}$, $\bullet\text{OOH}$, and $\bullet\text{CH}_3$, along with lines 3 and 4 from the six-line Mn^{2+} reference spectrum. Radical identification was based on hyperfine coupling constants from the Spin Trap Database of the National Institute of Environmental Health Sciences (NIEHS, USA).^[57]

Theoretical Methods—DFT+U Electronic Structure Calculations: Spin-polarized density functional theory (DFT) calculations were performed using the slab-supercell approach as implemented in the Vienna *Ab Initio* Simulation Package (VASP, versions 5.4.4, 6.3.0, and 6.4.2).^[58–60] The Perdew–Burke–Ernzerhof (PBE) generalized gradient approximation (GGA) was employed within the projector augmented wave (PAW) framework,^[61,62] with a plane-wave cutoff energy of 700 eV. The valence states included Fe (3p, 3d, 4s), O (2s, 2p), and H (1s), while core electrons were treated using the frozen-core approximation. To account for strong electron correlation in Fe 3d orbitals, a Hubbard U correction of 3.8 eV was applied within the PBE+U framework, consistent with previous studies.^[63,64] Long-range dispersion interactions were included via the DFT-D3 scheme.^[65,66]

The Fe_3O_4 (001) surface was modeled using the subsurface cation vacancy (SCV) reconstruction in a $(\sqrt{2}\times\sqrt{2})\text{R}45^\circ$ symmetry (Figure 3). The slab consisted of 13 atomic layers and a vacuum spacing of at least 15 Å, with in-plane lattice parameters fixed at 8.52 Å. A Monkhorst–Pack k-point grid of $4\times 4\times 1$ was used. All atomic positions were relaxed until forces were below 0.05 eV/Å and total energy changes were less than 1×10^{-5} eV.

The oxidation states of Fe cations were estimated based on their local magnetic moments, calculated as the difference between spin-up and spin-down electron densities integrated over spheres with radii chosen as the Wigner-Seitz radii of the PAW potentials. Magnetic moments of $\approx 3.7\mu_{\text{B}}$ and $\approx 4.1\mu_{\text{B}}$ were used to identify Fe^{3+} and Fe^{2+} , respectively (Table S1, Supporting Information). For Fe^{4+} , as in ferryl ($\text{Fe}^{4+}=\text{O}$) species, the magnetic moment ($\approx 3.4\mu_{\text{B}}$) closely overlaps with Fe^{2+} , so Bader charge analysis was employed to differentiate between these oxidation states (Table S1, Supporting Information). Table S2 (Supporting Information) reports the average distances between iron cations and their coordinated oxygen atoms in the dry SCV surface model, offering structural insight into the coordination geometry and oxidation states of the different Fe sites.

To approximate the aqueous environment, explicit water molecules were included in models of H_2O_2 decomposition on the reconstructed Fe_3O_4 (001) surface. One or three water molecules were added to the SCV model with adsorbed H_2O_2 . In the three-water model, a mixed molecular/dissociative adsorption configuration was used, with an additional water molecule hydrogen-bonded to a surface O(2c) atom, consistent with prior *ab initio* studies^[37,46] and favorable for interaction with reactive intermediates. To further assess bulk solvation effects, the three-water configurations were extended with the linearized, local implicit solvent model implemented in VASPsol+^[54] which accounts for electrostatic screening by the aqueous medium.

Geometries of reactants, products, and intermediates were optimized for both the hydroxyl and peroxy cleavage pathways, as well as for the formation of ferryl ($\text{Fe}^{4+}=\text{O}$) species. All optimizations were carried out on dry and hydrated SCV (001) models with zero, one, or three

water molecules. Transition states (TS) along the reaction coordinates were located using the climbing image nudged elastic band (CI-NEB) method,^[67,68] employing 6 to 18 images depending on pathway complexity. Each TS was validated by the presence of a single imaginary frequency (Table S4, Supporting Information).

To assess product desorption under aqueous conditions, additional structural optimizations were performed for adsorbed and desorbed states, including up to 12 explicit water molecules to represent solvation effects.

Supporting Information

Supporting Information is available from the Wiley Online Library or from the author.

Acknowledgements

V.M.S., E.L., and J.S.G. contributed equally to this work. The authors thank M. Meier and G. E. Murgida for helpful discussions on the estimation of iron cations' oxidation states, and T. Soteras for his involvement in the early stages of the research, particularly in reproducing the bulk and reconstructed Fe₃O₄ (001) surface, in accordance with the literature. J.S.G. gratefully acknowledges the National Agency for the Promotion of Research, Technological Development, and Innovation (Agencia I+D+i), Argentina, for fellowship support. M.V.G.P. and P.G.L. acknowledge funding from Grant PID2021-128915NB-I00, provided by MCIN/AEI/10.13039/501100011033 and co-financed by ERDF, EU. We also acknowledge the computational resources provided by the Red Española de Supercomputación (RES) at the MareNostrum 5 (BSC, Barcelona) node. This research was further supported by a Marie Skłodowska-Curie Actions grant under the NESTOR-H2020-MSCA-RISE-2020 project [Grant agreement ID: 101007629].

Conflict of Interest

The authors declare no conflict of interest.

Data Availability Statement

The data that support the findings of this study are available from the corresponding author upon reasonable request. The DFT data that support the findings of this study are available in Zenodo at <https://doi.org/10.5281/zenodo.17406050>.

Keywords

magnetite nanoparticles, nanozymes, fenton-like catalysis, ferryl intermediate, density functional theory calculations

Received: June 26, 2025
Revised: October 17, 2025
Published online: November 17, 2025

- [1] Z. Feng, Y. Guo, Y. Zhang, A. Zhang, M. Jia, J. Yin, G. Shen, *J. Nanobiotechnol.* **2024**, 22, 704.
- [2] L. Gao, H. Wei, S. Dong, X. Yan, *Adv. Mater.* **2024**, 36, 2305249.
- [3] Y. Ai, Z. e.-N. Hu, X. Liang, H.-B. Sun, H. Xin, Q. Liang, *Adv. Funct. Mater.* **2022**, 32, 2110432.

- [4] D. Jiang, D. Ni, Z. T. Rosenkrans, P. Huang, X. Yan, W. Cai, *Chem. Soc. Rev.* **2019**, 48, 1440.
- [5] G. F. Goya, A. Mayoral, E. Winkler, R. D. Zysler, C. Bagnato, M. Raineri, J. A. Fuentes-García, E. Lima Jr, *J. Appl. Phys.* **2021**, 130, 190903.
- [6] A. Robert, B. Meunier, *ACS Nano* **2022**, 16, 6956.
- [7] H. Fan, R. Zhang, K. Fan, L. Gao, X. Yan, *ACS Nano* **2024**, 18, 2533.
- [8] Z. Chen, J.-J. Yin, Y. u.-T. Zhou, Y. u. Zhang, L. Song, M. Song, S. Hu, N. Gu, *ACS Nano* **2012**, 6, 4001.
- [9] Q. Liu, A. Zhang, R. Wang, Q. Zhang, D. Cui, *Nanomicro Lett.* **2021**, 13, 154.
- [10] F. Chen, S. Xie, X. Huang, X. Qiu, *J. Hazard. Mater.* **2017**, 322, 152.
- [11] W. Sun, S. Wang, Z. Yu, X. Cao, *Environ. Sci. Water Res. Tech.* **2023**, 9, 1266.
- [12] Z. Chen, Y. Yu, Y. Gao, Z. Zhu, *ACS Nano* **2023**, 17, 13062.
- [13] M. A. Voinov, J. O. S. Pagán, E. Morrison, T. I. Smirnova, A. I. Smirnov, *J. Am. Chem. Soc.* **2011**, 35, 133.
- [14] L. Gao, K. Fan, X. Yan, *Theranostics* **2017**, 7, 3207.
- [15] S. Yu, H. Zhang, S. Zhang, M. Z. Fan, H. Fan, *Front. Chem.* **2021**, 9, 651053.
- [16] J.-J. Zheng, F. Zhu, N. Song, F. Deng, Q. i. Chen, C. Chen, J. He, X. Gao, M. Liang, *Nat. Protoc.* **2024**, 19, 3470.
- [17] L. Qiao, Z. Fu, J. Li, J. Ghosen, M. Zeng, J. Stebbins, P. N. Prasad, M. T. Swihart, *ACS Nano* **2017**, 11, 6370.
- [18] T. Cañeque, L. Baron, S. Müller, A. Carmona, L. Colombeau, A. Versini, S. Solier, C. Gaillet, F. Sindikubwabo, J. L. Sampaio, M. Sabatier, E. Mishima, A. Picard-Bernes, L. Syx, N. Servant, B. Lombard, D. Loew, J. Zheng, B. Proneth, L. K. Thoidingjam, L. Grimaud, C. S. Fraser, K. J. Szylo, E. D. Kazarian, C. Bonnet, E. Charafe-Jauffret, C. Ginestier, P. Santofimia-Castaño, M. Estaras, N. Dusetti, et al., *Nature* **2025**, 642, 492.
- [19] S. J. Dixon, J. A. T. C. B. F. Olzmann, *Nat. Rev. Mol. Cell Biol.* **2024**, 25, 424.
- [20] A. Gallo-Cordova, J. J. Castro, E. L. Winkler, E. Lima, R. D. Zysler, M. del Puerto Morales, J. G. Ovejero, D. A. Streitwieser, *J. Clean Prod.* **2021**, 308, 127385.
- [21] L. Lai, Y. He, H. Zhou, B. Huang, G. Yao, B. Lai, *J. Hazard. Mater.* **2021**, 416, 125809.
- [22] F. Haber, J. Weiss, *Proc. R. Soc. Lond. A Math. Phys. Sci.* **1934**, 147, 332.
- [23] W. C. Bray, M. H. F. I. O. N. Gorin, *J. Am. Chem. Soc.* **1932**, 54, 2124.
- [24] H. Dong, W. Du, J. Dong, R. Che, F. Kong, W. Cheng, M. Ma, N. Gu, Y. Zhang, *Nat. Commun.* **2022**, 13, 5365.
- [25] H. J. H. Fenton, *J. Chem. Soc., Trans.* **1894**, 65, 899.
- [26] W. G. Barb, J. H. Baxendale, P. George, K. R. Hargrave, *Trans. Faraday Soc.* **1951**, 47, 462.
- [27] W. G. Barb, J. H. Baxendale, P. George, K. R. Hargrave, *Trans. Faraday Soc.* **1951**, 47, 591.
- [28] N. Zheng, Y. Lian, Q. Zhou, R. Wang, X. He, R. Hu, Z. Hu, *Chem. Eng. J.* **2022**, 437, 135265.
- [29] P. R. Ortiz De Montellano, *Biocatalysis Based on Heme Peroxidases*, First Ed., (Eds.: E. Torres, M. Ayala), Springer, Berlin, **2010**, Ch 5.
- [30] T. G. Traylor, J. P. Ciccone, *J. Am. Chem. Soc.* **1989**, 111, 8413.
- [31] E. A. Jarvis, A. M. Chaka, *Surf. Sci.* **2007**, 601, 1909.
- [32] X.-G. Wang, W. Weiss, S. h. Shaikhutdinov, M. Ritter, M. Petersen, F. Wagner, R. Schlögl, M. T. H. Scheffler, *Phys. Rev. Lett.* **1998**, 81, 1038.
- [33] K. Wan, B. Jiang, T. Tan, H. Wang, M. Liang, *Small* **2022**, 18, 2204372.
- [34] B. Arndt, R. Bliem, O. Gamba, J. E. S. Van Der Hoeven, H. Noei, U. Diebold, G. S. Parkinson, A. Stierle, *Surf. Sci.* **2016**, 653, 76.
- [35] R. Bliem, E. McDermott, P. Ferstl, M. Setvin, O. Gamba, J. Pavelec, M. A. Schneider, M. Schmid, U. Diebold, P. Blaha, L. Hammer, G. S. Parkinson, *Science* **2014**, 346, 1215.

- [36] E. Zaki, Z. Jakub, F. Mirabella, G. S. Parkinson, S. Shaikhutdinov, H. J. Freund, *J. Phys. Chem. Lett.* **2019**, *10*, 2487.
- [37] M. Meier, J. Hulva, Z. Jakub, J. Pavelec, M. Setvin, R. Bliem, M. Schmid, U. Diebold, C. Franchini, G. S. Parkinson, *Proc. Natl. Acad. Sci. USA* **2018**, *115*, E5642.
- [38] P. Sombut, M. Meier, M. Eder, T. Angerler, O. Gamba, M. Schmid, U. Diebold, C. Franchini, G. S. Parkinson, *The Surface Phase Diagram of Fe₃O₄(001) Revisited*, RSC Applied Interfaces, Cambridge **2025**, pp. 673–683.
- [39] M. Hermanek, R. Zboril, I. Medrik, J. Pechousek, C. Gregor, *J. Am. Chem. Soc.* **2007**, *129*, 10929.
- [40] P. J. Lin, C. H. Yeh, J. C. Jiang, *RSC Adv.* **2021**, *11*, 36257.
- [41] X. Shen, Z. Wang, X. J. Gao, X. Gao, *Adv. Mater.* **2024**, *36*, 2211151.
- [42] X. Shen, Z. Wang, X. Gao, Y. Zhao, *ACS Catal.* **2020**, *10*, 12657.
- [43] S. Guo, L. Guo, *J. Phys. Chem. C* **2019**, *123*, 30318.
- [44] P. Siani, E. Bianchetti, H. Liu, C. Di Valentin, *J. Chem. Phys.* **2021**, *154*, 034702.
- [45] H. Liu, E. Bianchetti, P. Siani, C. Di Valentin, *J. Chem. Phys.* **2020**, *152*, 124711.
- [46] S. Romano, P. Montero de Híjes, M. Meier, G. Kresse, C. Franchini, C. Dellago, *J. Chem. Theory Comput.* **2025**, *21*, 1951.
- [47] C. Liang, S. Huang, W. Zhao, W. Liu, J. Chen, H. Liu, Y. Tong, *New J. Chem.* **2015**, *39*, 2651.
- [48] B. A. Wechsler, D. H. Lindsley, C. T. Prewitt, *Am. Mineral.* **1984**, *69*, 754.
- [49] C. Pecharrmán, T. González-Carreño, J. E. Iglesias, *Phys. Chem. Miner.* **1995**, *22*.
- [50] A. C. Moreno Maldonado, E. L. Winkler, M. Raineri, A. Toro Córdova, L. M. Rodríguez, H. E. Troiani, M. L. Mojica Piscioti, M. V. Mansilla, D. Tobia, M. S. Nadal, T. E. Torres, E. De Biasi, C. A. Ramos, G. F. Goya, R. D. Zysler, E. Lima, *J. Phys. Chem. C* **2019**, *123*, 20617.
- [51] M. Raineri, E. L. Winkler, T. E. Torres, M. Vasquez Mansilla, M. S. Nadal, R. D. Zysler, E. Lima, *Nanoscale* **2019**, *11*, 18393.
- [52] J. M. D. Coey, *Magnetism and Magnetic Materials*, Cambridge University Press, Cambridge **2001**.
- [53] V. Vacque, B. Sombret, J. P. Huvenne, P. Legrand, S. Suc, *Spectrochim. Acta A Mol. Biomol. Spectrosc.* **1997**, *53*, 55.
- [54] K. Mathew, R. Sundararaman, K. Letchworth-Weaver, T. A. Arias, R. G. Hennig, *J. Chem. Phys.* **2014**, *140*, 084106.
- [55] L. Gao, J. Zhuang, L. Nie, J. Zhang, Y. Zhang, N. Gu, T. Wang, J. Feng, D. Yang, S. Perrett, X. Yan, *Nat. Nanotechnol.* **2007**, *2*, 577.
- [56] R. Vasquez-Medrano, D. Prato-Garcia, M. Vedrenne, *Adv. Oxid. Processes Waste Water Treatment*, (Eds.: S. C. Ameta, R. Ameta) Academic press, **2018**, pp 89–113.
- [57] Spin Trap Database. <https://www.niehs.nih.gov/research/resources/databases/spintrap> (accessed **2025** September).
- [58] VASP. <https://www.vasp.at/> (accessed **2025** September).
- [59] G. Kresse, J. Hafner, *Phys. Rev. B* **1993**, *48*, 13115.
- [60] G. Kresse, J. Furthmüller, *Phys. Rev. B* **1996**, *54*, 11169.
- [61] J. P. Perdew, K. Burke, M. Ernzerhof, *Phys. Rev. Lett.* **1996**, *77*, 3865.
- [62] G. Kresse, D. Joubert, *Phys. Rev. B* **1999**, *59*, 1758.
- [63] X. Yu, C. F. Huo, Y. W. Li, J. Wang, H. Jiao, *Surf. Sci.* **2012**, *606*, 872.
- [64] S. L. Dudarev, G. A. Botton, S. Y. Savrasov, C. J. Humphreys, A. P. Sutton, *Phys. Rev. B* **1998**, *57*, 1505.
- [65] S. Grimme, J. Antony, S. Ehrlich, H. Krieg, *J. Chem. Phys.* **2010**, *132*, 154104.
- [66] S. Grimme, S. Ehrlich, L. Goerigk, *J. Comput. Chem.* **2011**, *32*, 1456.
- [67] G. Mills, H. Jónsson, G. K. Schenter, *Surf. Sci.* **1995**, *324*, 305.
- [68] H. Jónsson, G. Mills, K. W. Jacobsen, *Classical Quantum Dynam. Condensed Phase Simulat* (Eds.: B. J. Berne, G. Ciccotti, D. F. Coker), World Scientific **1998**, 385.